■ Ionic Conductors
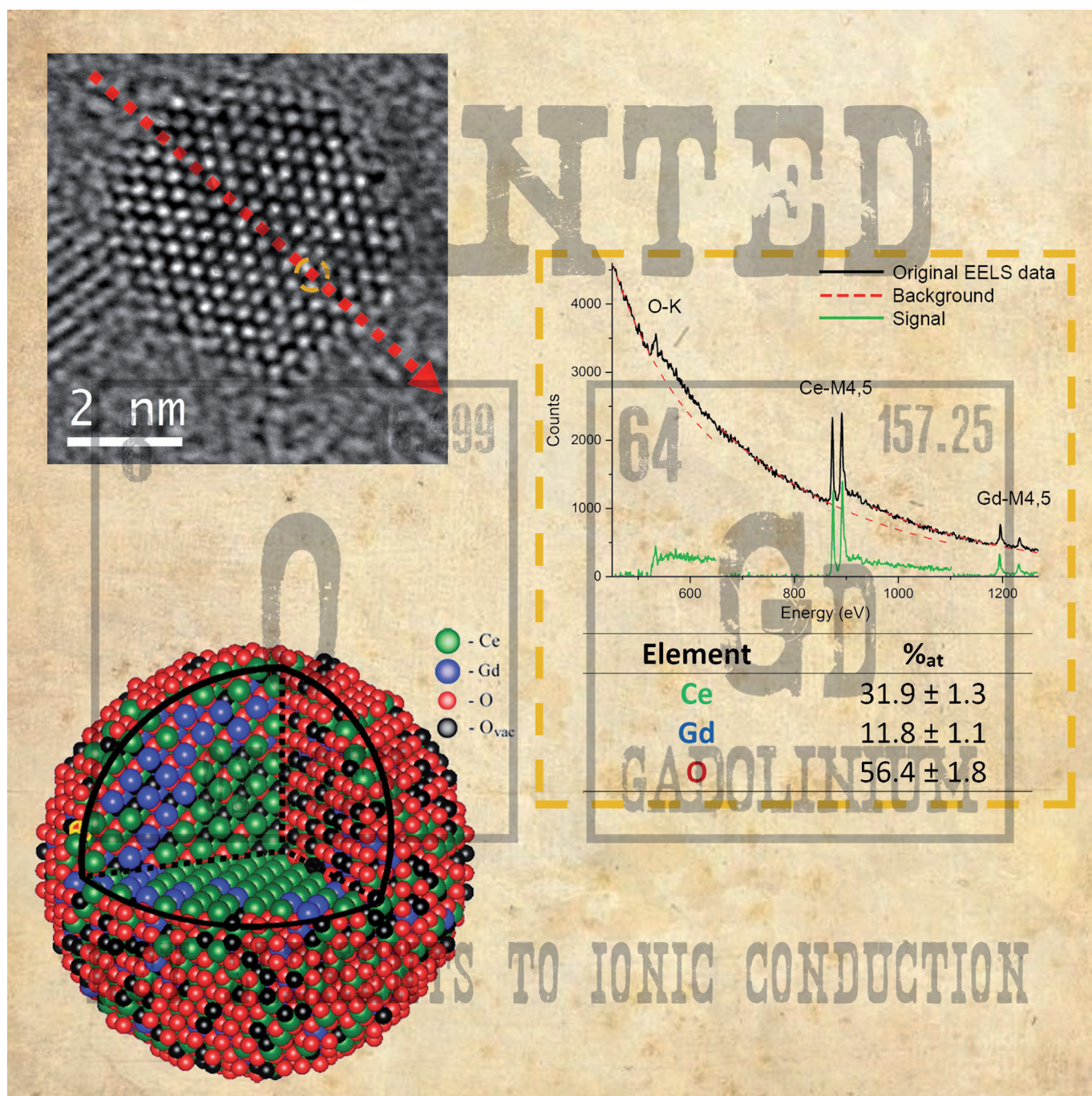
Analysis of Dopant Atom Distribution and Quantification of Oxygen Vacancies on Individual Gd-Doped CeO₂ Nanocrystals

Daniel G. Stroppa,*[a, b, e] Cleocir J. Dalmaschio,[c, f] Lothar Houben,[a] Juri Barthel,[a, d] Luciano A. Montoro,[b] Edson R. Leite,[c] and Antonio J. Ramirez[b]

Abstract: This work reports the analysis of the distribution of Gd atoms and the quantification of O vacancies applied to individual CeO_2 and Gd-doped CeO_2 nanocrystals by electron energy-loss spectroscopy. The concentration of O vacancies measured on the undoped system ($6.3 \pm 2.6\%$) matches the expected value given the typical Ce^{3+} content previously reported for CeO_2 nanoparticles. The doped nanoparticles have an uneven distribution of dopant atoms and an atypical amount of O vacant sites ($37.7 \pm 4.1\%$). The measured decrease of the O content induced by Gd doping cannot be explained solely by the charge balance including Ce^{3+} and Gd^{3+} ions.

Introduction

Oxygen vacancies are responsible for many interesting properties of oxide materials, and their controlled manipulation can lead to remarkable technological impact. Many applications, including solid oxide fuel cells (SOFCs),[1] catalysts,[2] sensors,[3] and optoelectronic devices,[4] depend on the amount of equilibrium O vacancies, their localization, and mobility.[5] Possible approaches to control these features are related to altering the crystalline structure,[6] the particle size,[7] and the composition by doping the material with lower valence cations.[8]

The direct measurement of O self-diffusion and surface exchange is a common practice to evaluate ionic conductive materials.[9] For nanostructured systems, however, the typical dimensions preclude similar measurements and also make intricate the use of standard characterization techniques aiming the O quantification. Even though experimental approaches based on X-rays diffraction (XRD)[10] and Raman spectroscopy[11] can provide an average O quantification for relatively large sample volumes, their limited spatial resolution precludes local measurements on nanosized systems.

Few examples of O concentration measurement with high spatial resolution using high-resolution transmission electron microscopy (HRTEM)[12, 13] and high-resolution scanning transmission electron microscopy (HRSTEM)[14, 15] approaches have been reported. Even though these characterization techniques have shown quantitative results for individual atomic columns[13] and sensitivity for the detection of O vacancies on the concentration range of 1–4%,[14] their application to individual nanocrystals is generally problematic. The main reasons are 1) the complexity of representing nanoparticles at the atomic level to carry out HRTEM simulations quantitatively, and 2) particle instability that prevents high signal-to-noise spectroscopy analysis and accurate measurement of local lattice distortions on 0D materials by HRSTEM.

We present a quantitative characterization of CeO_2 and Gd-doped CeO_2 (CGO) nanocrystals aiming to evaluate the distribution of dopant atoms and the concentration of O vacancies on individual nanocrystals. For this purpose we combine the relative quantification of chemical species by high-spatial-resolution electron energy-loss spectroscopy (EELS) with a modeling procedure based on the HRTEM imaging results. The investigation of the CeO_2 system is motivated by its promising performance as a low-temperature ionic conductor in SOFCs, which is notably enhanced by Gd doping on the $10–20\%_{at}$ range.[16]

Results

CeO_2 and CGO nanocrystals were initially analysed by HRTEM. Example images of typical nanoparticles are displayed in Figure 1. Average nanocrystals sizes of (6.8 ± 1.8) and (5.5 ± 1.3) nm were measured for the undoped and the doped systems, respectively. Average interplanar distances extracted from Fourier transforms (FT) of HRTEM images indicate that both systems have the CeO_2 cubic crystallographic structure,[17] and that Gd-doping does not lead to a significant lattice distortion within the measurement precision (± 0.024 nm). Powder X-ray diffraction (XRD) and Raman spectroscopy results

[a] Dr. D. G. Stroppa, Dr. L. Houben, Dr. J. Barthel
Ernst Ruska-Centre, Forschungszentrum Jülich
52425 Jülich (Germany)

[b] Dr. D. G. Stroppa, Prof. L. A. Montoro, Dr. A. J. Ramirez
Brazilian Nanotechnology National Laboratory
13083-970, Campinas, SP (Brazil)

[c] Prof. C. J. Dalmaschio, Prof. E. R. Leite
Department of Chemistry, Federal University of São Carlos
13565-905, São Carlos (Brazil)

[d] Dr. J. Barthel
Central Facility for Electron Microscopy
RWTH Aachen University, 52074 Aachen (Germany)

[e] Dr. D. G. Stroppa
Current position: International Iberian Nanotechnology Laboratory (INL)
Braga (Portugal)
E-mail: daniel.stroppa@inl.int

[f] Prof. C. J. Dalmaschio
Current position: Universidade Federal do Espírito Santo (UFES)
São Mateus (Brazil)
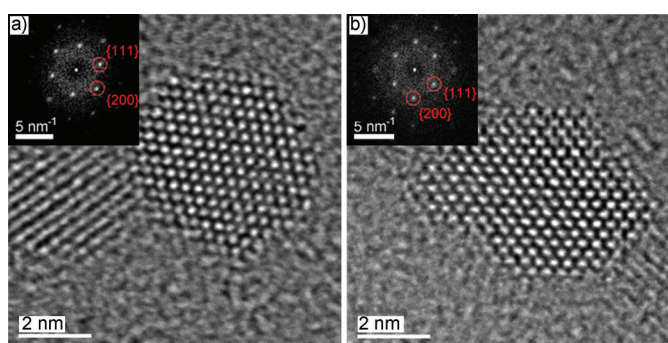
Figure 1. HRTEM images of typical a) CeO_2 and b) CGO nanocrystals. The corresponding FT analyses (insets) indicate interplanar spacings pertinent to the CeO_2 cubic crystalline structure.

show that the studied systems possess only the referred crystalline phase.

CeO$_2$ nanocrystal characterization by EELS

Figure 2 presents results for the CeO$_2$ nanocrystals characterization by STEM-EELS. Line profiles with equidistantly spaced measurement points were acquired for ten different CeO$_2$ nanoparticles. A small undersampling of the O concentration
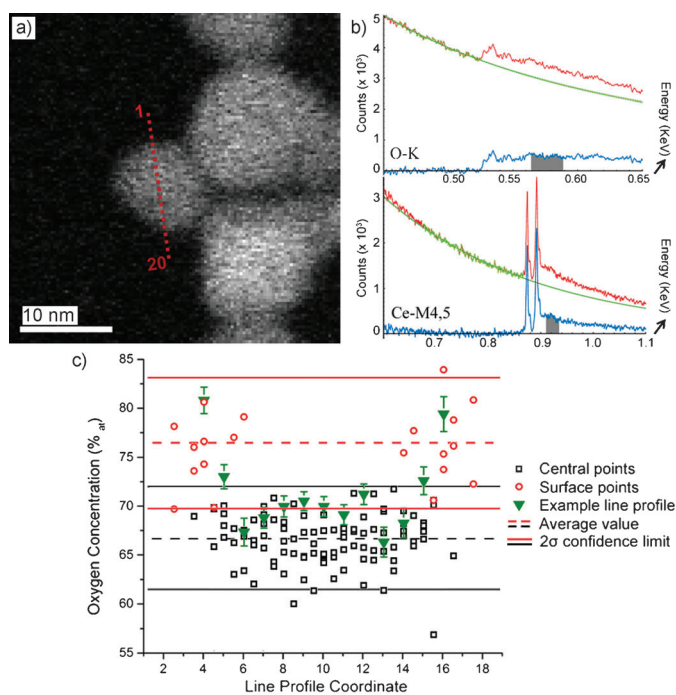
Figure 2. CeO$_2$ nanocrystals quantitative analysis. a) HAADF image indicating the location of an EELS line-profile measurement. b) O-K and Ce-M4,5 energy losses regions on the EEL spectrum of a sample point on the depicted line profile. The original spectrum (red), the background fit (green) and the signal integration region (grey) on the background subtracted data (blue) are denoted. c) Measured O concentration profile for 10 different CeO$_2$ nanocrystals. O rich regions on nanoparticles surfaces (red) are distinguishable from the central points (black) for every line-profile measurement.

profile is used, since the average interspacing on the line-profile measurement points (0.6 nm) is larger than the approximate EELS interaction diameter (0.4 nm) for the used experimental configuration.

The EELS results displayed in Figure 2c indicate an O enrichment at the CeO$_2$ nanocrystals surface. This observation is expected given the results from FT infrared spectroscopy (FT-IR) and thermogravimetric analysis (TGA), which indicates the presence of OH-bonded radicals. This is predictable due to the basic environment from the co-precipitation synthesis procedure.

An average O relative ratio of $(66.9 \pm 3.6)\%_{at}$ is obtained by taking into account the central points (indicated as black squares on Figure 2c) of the 10 line-profile measurements, while an average error of 1.2 $\%_{at}$ was estimated for the O quan-

tification of an EEL single spectrum. As the dispersion on the O content of CeO$_2$ nanocrystals is higher than the estimated quantification error, an intrinsic heterogeneity of undoped system is indicated. However, no correlation is observed between the relative O content and the measured particles size.

CGO nanocrystal characterization by EELS

Figure 3 shows the Gd and O concentration profiles obtained for the CGO nanocrystals by the EEL spectra quantification. Similar to the characterization of CeO$_2$ nanocrystals, EELS spectra were obtained from equidistantly spaced measurement points applied to 20 different CGO nanocrystals.

The concentration profiles obtained for the CGO system, displayed in Figure 3c, indicates an uneven distribution of Gd dopant atoms, and a significant reduction of the O net content with respect to the undoped system. The presence of O-rich surface terminations is also observed in this system.

An average Gd relative ratio of $(26.4 \pm 4.9)\%_{at}$ is obtained considering all the points on each of the 20 line-profile measurements of CGO nanocrystals, while an average error of 2.6 $\%_{at}$ was estimated for the Gd quantification of an individual
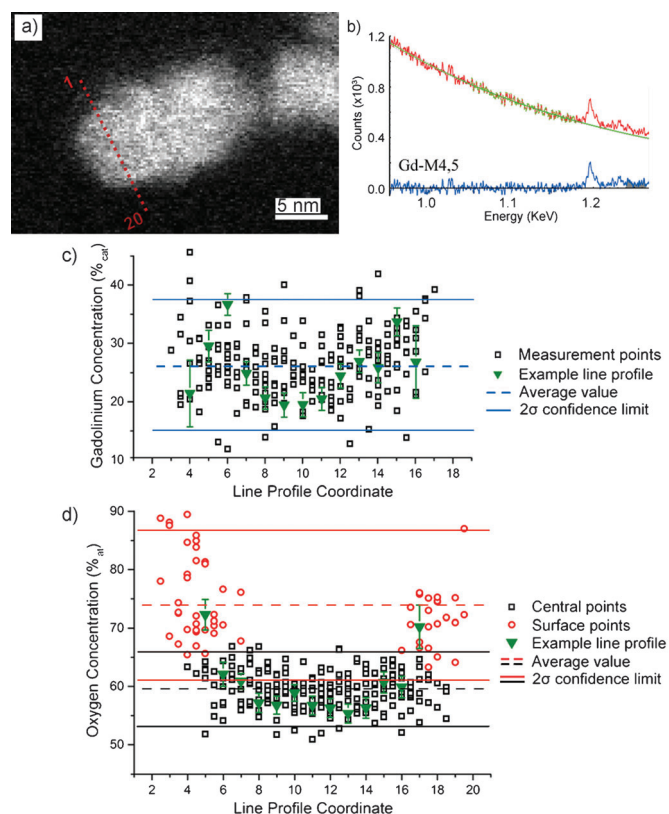
Figure 3. CGO nanocrystals quantitative analysis. a) HAADF image indicating the location of an EELS line-profile measurement. b) Gd-M4,5 energy loss region on the EELS spectrum of a sample point on the depicted line profile. The original spectrum (red), the background fit (green) and the signal integration region (grey) on the background subtracted data (blue) are denoted. The Ce-M4,5 and O-K spectrum regions are omitted due to similarity in comparison to the ones present in Figure 2b. Quantitative results on the c) Gd and d) O concentration profile on 20 different CGO nanocrystals.

EEL spectrum. With respect to the O relative ratio, an overall value of $(59.5 \pm 2.8)\%_{at}$ is obtained by taking into account the central points (indicated as black squares on Figure 3c) of the 20 line-profile measurements, while an average error of $1.6\%_{at}$ was estimated for the quantification of a single spectrum. As the EELS quantification error is significantly smaller then observed dispersion of the Gd and O relative contents, an intrinsic variability in the composition of the analyzed CGO nanoparticles is indicated. Again, a correlation between measured particles size and their average content of Gd and O is not observed.

Discussion

A model-based approach was used to convert the projected local concentration provided by the line-profile measurements into three-dimensional distributions of dopants and O vacancies. Two reasons justify the use of models to describe the investigated systems. The first is to provide a direct interpretation of the quantitative results by compensating the projection effect and weighting the measured composition with respect to the estimated local thickness. This is important since the quantification of each point on the line profile takes into account only the ratio of atomic species within the interaction volume for that probing location, without accounting for the local thickness. The second reason is to translate the line-profile results in a 3D representation of the nanocrystals. The use of spherical models is a reasonable approximation for this purpose given the observed nanocrystals morphology and the high degree of symmetry from the CeO_2 unit cell.

CeO_2 nanocrystals modeling

Results obtained by applying the spherical model to evaluate the O concentration profile for an individual CeO_2 nanocrystal are depicted in Figure 4. The fit data for the O site occupancy indicates an almost uniform O distribution over the nanoparticles. A fraction of unoccupied O sites of $(5.8 \pm 2.1)\%$ is obtained for the depicted example. The average O vacancy concentration of the CeO_2 system is evaluated as $(6.3 \pm 2.6)\%$ taking two aspects into consideration. First is the observed spread on the average O ratio for different CeO_2 nanocrystals (Figure 2c). Second is the average O content from the depicted example in comparison to the line-profile quantification results for the other measured nanoparticles.

The O vacancy concentration that we obtain experimentally is in good agreement with the O equilibrium vacancies that typically occur on nanostructured CeO_2 to promote the charge balance due to the presence of Ce^{3+} ions. The present values agree well with the Ce^{3+} content reported in the literature by Deshpande et al.[18] and Babu et al.,[11] which indicate O vacancies concentrations of 7.2 and 8.6%, respectively, for systems with 6 and 3.7 nm average particles size, respectively. It is worth mentioning that the Ce^{3+} content is expected to increase for reduced particle sizes.[7] The agreement between the measurements indicates that the EELS quantification and mod-
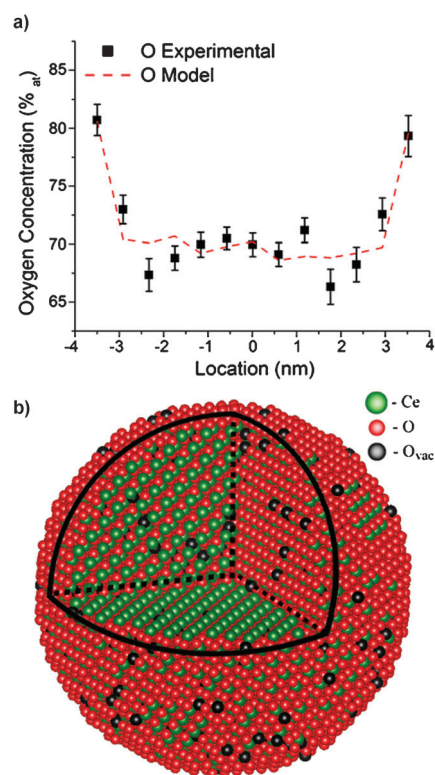
Figure 4. CeO_2 nanoparticle modeling. a) Experimentally measured O concentration profile (black squares) and simulated profile (dashed line) considering a spherical nanoparticle model. b) Corresponding atomic model resulting from the O site occupancy fitting. The missing octant representation is used for illustrative purposes only to aid the O vacancy distribution visualization.

eling procedure applied here provides a reasonable quantification of O vacancies for individual nanoparticles.

CGO nanocrystals modeling

Results from the modeling applied to the Gd and O concentration profiles of an example CGO nanocrystal are depicted in Figure 5. The Gd dopant atom distribution is uneven, with a noticeable tendency for surface enrichment. This can be understood as a mechanism for the surface energy minimization, since the migration of dopant atoms with lower oxidation towards to the surface tends to compensate the surface dangling bonds.

An overall Gd concentration $(29.1 \pm 1.5)\%$ is obtained for the depicted example, whereas the overall Gd concentration over the many evaluated CGO nanocrystals is $(30.0 \pm 8.2)\%$. The uncertainty in Gd quantification here is due to a combination of the quantification error and the intrinsic variability of the evaluated nanoparticles (Figure 3c). The discrepancy between measured (30%) and expected Gd dopant content (20%) can be explained by the difference of the solubility products of the intermediary Ce and Gd hydroxide compounds formed during the reaction.

The O distribution evaluated for the CGO nanoparticles is almost uniform, similar to the CeO_2 nanocrystalline system.
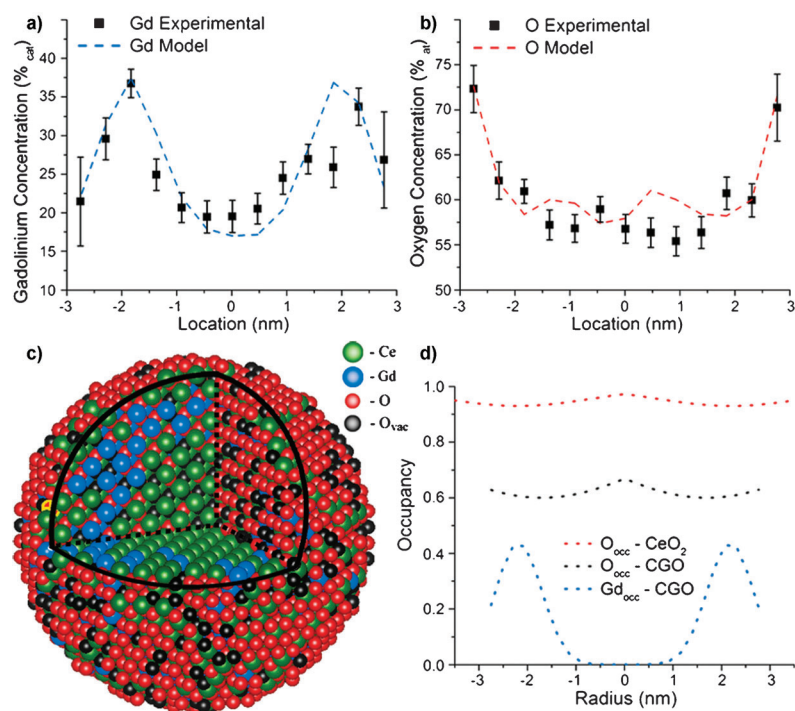
Figure 5. CGO nanoparticle modeling. Experimentally measured a) Gd and b) O concentration profiles (black squares), and the respective simulated profiles (dashed lines) considering a spherical nanoparticle model. c) Corresponding atomic model resulting from the Gd and O site occupancy fitting. d) Comparison of the fitting functions obtained for O and Gd occupancy on undoped and doped nanocrystals.

However, a remarkable reduction of the average O site occupation is observed. While a value of $(38.6 \pm 2.4)\%$ is obtained for unoccupied O sites for the depicted example, the average O vacancy concentration for the 20 measured CGO nanoparticles is evaluated as $(37.7 \pm 4.1)\%$.

Table 1 presents a summary of the experimental quantification results obtained by modeling of EELS line profiles and the theoretical predictions based on the charge equilibrium for stoichiometric CeO_2 structures. The comparison shows that the O deficiency measured for the CGO system cannot be solely explained by the electrical charge balance, considering the measured concentration of Gd^{3+} dopant atoms and the amount of Ce^{3+} ions expected due to the particles size and the Gd doping level.[11] In such scenario, the expected maximum amount of vacant O sites would be only 13.8%.

Even though Ce and Gd atoms could have lower oxidation states than $3+$,[19] these configurations only occur for extreme synthesis conditions and are unlikely given the cations' oxida-

tion state from the precursor materials used in the synthetic procedure. In addition, different crystalline phases than those identified by HRTEM and XRD would be expected in the presence of such cations.

The O deficiency measured for CGO nanocrystals cannot be explained by a dissimilar behavior of O knock-on damage or diffusion between doped and undoped nanocrystals. The maximum transferable energy from 80 kV incident electrons to O atoms is about 14 eV,[20] which is well below the typical threshold displacement energy of 25 eV. It is worth noting that this typical value may vary for different bonding configurations; nevertheless the Ce—O bond strength should not be affected to a great extent by the presence of a neighboring Gd atom or an O vacant site. For this reason, other effects which depend on the bond strength, such as sputtering damage or local heating, can be ruled out as main explanations for the excess of vacancies induced by doping.

Other possible explanation for the unexpectedly high amount of O vacancies induced by doping would be related to the formation of a superstructure lattice consisting of the CeO_2 crystallographic structure with periodic O defects. This hypothesis can be ruled out given the absence of noticeable intensity modulation on HRTEM, high-resolution high-angle annular dark field (HAADF), and ADF STEM images from nanoparticles on different zone axes.

At present, a complete explanation for the unusual amount of O vacancies induced by Gd doping on CeO_2 nanocrystals is not available in the literature to our knowledge. The most likely hypothesis is that the high dopant concentration combined with the low association enthalpy (HA) from the GdVO' pair (0.12 eV)[21] may promote the stability of such positively charged couples, and consequently a net electric charge misbalance. In this scenario, the O excess on the nanoparticles surfaces and the observed distribution of dopant atoms may contribute to the system stabilization.

Conclusion

Oxygen vacancy and dopant concentration profiles were measured quantitatively in individual CeO_2 and Gd-doped CeO_2 nanoparticles. A discrepancy between expected and experimentally measured oxygen vacancy concentrations for the Gd-doped CeO_2 challenges the presumption of charge balance in a strictly ionic model. This finding indicates the importance of

Table 1. Summary of experimental results and theoretical predictions for O vacancies concentration.

experimental		Gd [%at]	VO [%sites]
CeO_2		–	(6.3 ± 2.6)
CGO		(30.0 ± 8.2)	(37.7 ± 4.1)
theoretical	Ce^{3+} [%at]	Gd [%at]	V_O [%sites]
CeO_2	29.0	–	7.2
CGO	25.2	30.0	13.8

quantitative analyses with high spatial resolution for the development of reliable models to describe dopant atom segregation[22] and O defects at nanoscale. This knowledge may indicate novel approaches to attain materials with improved ionic transport properties[23] and open up new possibilities, such as the use of self-assembled systems, for related applications.

Experimental Section

CeO$_2$ and CGO nanoparticles syntheses were carried out by co-precipitation at room temperature.[24] Stoichiometric amounts of cations nitrites, aiming for 0% and 20% Gd cation ratios, respectively, were diluted to a 0.1 M aqueous solution, and then NH$_4$OH was added. The resulting solutions were washed and diluted with de-ionized water, placed in autoclave vessels; and thermally treated to 130 °C into a microwave oven for 30 min.

Electron microscopy samples were prepared by dropping CeO$_2$ and CGO nanocrystals aqueous solutions onto copper grids covered with a thin amorphous carbon film. Prior to the electron microscopy experiments, the prepared grids were kept in a vacuum chamber (10^{-3} Pa) for 4 h at 80 °C to minimize the sample contamination by carbon-based compounds.

HRTEM characterization was performed using a FEI TITAN 80–300 microscope equipped with image aberration-corrector and a Schottky field-emission electron gun operating at 300 kV. The images were recorded using the negative Cs imaging (NCSI) mode[25] providing 80 pm spatial resolution.

STEM characterization was carried out using a FEI TITAN 50–300 microscope equipped with probe aberration-corrector and a Schottky field-emission electron gun operating at 80 kV. Energy-loss spectra were recorded with a 0.2 nm diameter electron beam of approximate 0.1 nA current. Line-profile measurements were performed across individual nanoparticles with a 10 s collection time per EELS spectrum. High-angle annular dark field (HAADF) images were acquired prior and after the EELS spectra collection to check for visible damage of the samples induced by the electron beam during the experiments.

The signal of element-specific core losses was quantified after the EEL spectra background fitting and subtraction. Integration windows selecting the continuum states regions above the onset of Ce-M4,5, Gd-M4,5, and O-K transitions were chosen. The chemical species ratios were retrieved from the integrated intensities taking into account inelastic cross-sections, which have been measured using a CGO reference sample. The interaction volume was adjusted according to the transitions delocalization[26] for the spectra quantification.

Spherical atomistic models were used to interpret the EELS line-profile results. Structures with 7 and 5.5 nm were constructed[27] for representing the investigated CeO$_2$ and CGO nanocrystalline systems, respectively. The models include O-rich surface terminations and variable Ce and O atomic site occupancies. The occupancies were fitted by carrying out line-profile simulations applied to the models and verifying their adjustment to experimental line profiles. The local composition of every simulated line-profile point was calculated as the ratio of occupied sites within the effective interaction volume. Ce and O site occupancies were adjusted as a function of distance from the center of the models as normal distributions. Complementary Ce and Gd site occupation was considered for the Ce sites on the model structures, while the O sites could either contain an O atom or a vacancy.

[1] A. J. Jacobson, *Chem. Mater.* **2010**, *22*, 660–667.
[2] F. Esch, S. Fabris, L. Zhou, T. Montini, C. Africh, P. Fornasiero, G. Comelli, R. Rosei, *Science* **2005**, *309*, 752–755.
[3] M. Epifani, J. D. Prades, E. Comini, E. Pellicer, M. Avella, P. Siciliano, G. Faglia, A. Cirera, R. Scotti, F. Morazzoni, J. R. Morante, *J. Phys. Chem. C* **2008**, *112*, 19540–19546.
[4] M. Vasilopoulou, A. M. Douvas, D. G. Georgiadou, L. C. Palilis, S. Kennou, L. Sygellou, A. Soultati, I. Kostis, G. Papadimitropoulos, D. Davazoglou, P. Argitis, *J. Am. Chem. Soc.* **2012**, *134*, 16178–16187.
[5] H. Tuller, *Handbook of Electronic and Photonic Materials*, Springer, New York, **2006**, pp. 213–228.
[6] H. Hojo, T. Mizoguchi, H. Ohta, S. D. Findlay, N. Shibata, T. Yamamoto, Y. Ikuhara, *Nano Lett.* **2010**, *10*, 4668–4672.
[7] L. Wu, H. J. Wiesmann, A. R. Moodenbaugh, R. F. Klie, Y. Zhu, D. O. Welch, M. Suenaga, *Phys. Rev. B* **2004**, *69*, 125415.
[8] N. Shehata, K. Meehan, M. Hudait, N. Jain, *J. Nanopart. Res.* **2012**, *14*, 1173.
[9] P. S. Manning, J. D. Sirman, J. A. Kilner, *Solid State Ionics* **1996**, *93*, 125–132.
[10] A. Gayen, K. R. Priolkar, A. K. Shukla, N. Ravishankar, M. S. Hegde, *Mater. Res. Bull.* **2005**, *40*, 421–431.
[11] S. Babu, R. Thanneeru, T. Inerbaev, R. Day, A. E. Masunov, A. Schulte, S. Seal, *Nanotechnology* **2009**, 085713.
[12] H. Shibahara, K. Numaguchi, M. Kawasaki, H. Takizawa, T. Oikawa, H. Taguchi, *J. Electron Microsc.* **1995**, *44*, 174–181.
[13] C. L. Jia, K. Urban, *Science* **2004**, *303*, 2001–2004.
[14] D. A. Muller, N. Nakagawa, A. Ohtomo, J. L. Grazul, H. Y. Hwang, *Nature* **2004**, *430*, 657–661.
[15] Y.-M. Kim, J. He, M. D. Biegalski, H. Ambaye, V. Lauter, H. M. Christen, S. T. Pantelides, S. J. Pennycook, S. V. Kalinin, A. Y. Borisevich, *Nat. Mater.* **2012**, *11*, 888–894.
[16] B. C. H. Steele, *Solid State Ionics* **2000**, *129*, 95–110.
[17] M. Wołxcyrz, L. J. Kepinski, *J. Solid State Chem.* **1992**, *99*, 409–413.
[18] S. Deshpande, S. Patil, S. V. N. T. Kuchibhatla, S. Seal, *Appl. Phys. Lett.* **2005**, *87*, 133113.
[19] J. M. Leger, N. Yacoubi, J. Loriers, *Mater. Res. Bull.* **1979**, *14*, 1431–1436.
[20] D. B. Willians, C. B. Carter, *Transmission Electron Microscopy—A Textbook for Materials Science*, Springer, New York, **2009**; p. 62.
[21] R. Gerhardt, W.-K. Lee, A. S. Nowick, *J. Phys. Chem. Solids* **1987**, *48*, 563–569.
[22] D. G. Stroppa, L. A. Montoro, A. Beltrán, T. G. Conti, R. O. Da Silva, J. Andrés, E. R. Leite, A. J. Ramirez, *Chem. Eur. J.* **2011**, *17*, 11515–11519.
[23] S. Hui, J. Roller, S. Yick, X. Zhang, C. Deces-Petit, Y. Xie, R. Maric, D. Ghosh, *J. Power Sources* **2007**, *172*, 493–502.
[24] M. J. Godinho, R. F. Gonçalves, L. P. S. Santos, J. A. Varela, E. Longo, E. R. Leite, *Mater. Lett.* **2007**, *61*, 1904–1907.
[25] C.-L. Jia, M. Lentzen, K. Urban, *Microsc. Microanal.* **2004**, *10*, 174–184.
[26] R. F. Egerton, *Electron Energy-Loss Spectroscopy in the Electron Microscope*, 2nd ed., Plenum, New York, **1996**.
[27] D. G. Stroppa, R. D. Righetto, L. A. Montoro, A. J. Ramirez, *Ultramicroscopy* **2011**, *111*, 1077–1082.